Ionic/Electronic Conductivity, Thermal/Chemical Expansion and Oxygen Permeation in Pr and Gd Co-Doped Ceria PrxGd0.1Ce0.9-xO1.95-

Cheng, Shiyang; Chatzichristodoulou, Christodoulos; Søgaard, Martin; Kaiser, Andreas; Hendriksen, Peter Vang

Published in:
Journal of the Electrochemical Society

Link to article, DOI:
10.1149/2.0531713jes

Publication date:
2017

Document Version
Publisher's PDF, also known as Version of record

Ionic/Electronic Conductivity, Thermal/Chemical Expansion and Oxygen Permeation in Pr and Gd Co-Doped Ceria $Pr_xGd_{0.1}Ce_{0.9-x}O_{1.95-\delta}$

Shiyang Cheng,[z] Christodoulos Chatzichristodoulou, Martin Søgaard, Andreas Kaiser, and Peter Vang Hendriksen[*,z]

Department of Energy Conversion and Storage, Technical University of Denmark, DTU Risø campus, DK-4000 Roskilde, Denmark

The oxygen permeation flux of $Ce_{0.9}Gd_{0.1}O_{1.95-\delta}$ (CGO)-based oxygen transport membranes under oxidizing conditions is limited by the electronic conductivity of the material. This work aims to enhance the bulk ambipolar conductivity of CGO by partial substitution of Ce with the redox active element Pr. A series of compositions of $Pr_xGd_{0.1}Ce_{0.9-x}O_{1.95-\delta}$ (x = 0, 0.02, 0.05, 0.08, 0.15, 0.25, 0.3 and 0.4) was prepared by solid state reaction. X-ray powder diffraction (XPD) indicates that Pr is completely dissolved in the fluorite structure up to 40 at.%. Pronounced nonlinear thermal expansion behavior was observed as a function of temperature, due to the simultaneous contributions of both thermal and chemical expansion. The electronic and ionic conductivities were measured as a function of temperature and oxygen partial pressure. Within the range from 10 to 15 at.% Pr, a drastic drop of the activation energy of the hole mobility and an abrupt increase of the hole conductivity at low temperature was observed. The behavior could be rationalized by a simple percolation model. Oxygen permeation fluxes through disk shaped samples fed with air on one side and N_2 on the other side were also measured. The oxygen flux through $Pr_{0.05}Gd_{0.1}Ce_{0.85}O_{1.95-\delta}$ was higher than that for CGO by one order of magnitude owing to the enhanced electronic conductivity albeit the flux is still limited by the electronic conductivity. In terms of the electronic and ionic conductivity, the estimated maximum oxygen permeation flux of a 10 μm $Pr_{0.4}Gd_{0.1}Ce_{0.9}O_{1.95-\delta}$ -based membrane exceeds 10 Nml cm^{-2} min^{-1} at 900°C under a small oxygen potential gradient (0.21/10^{-3} bar) which is promising for use in oxygen production and in oxy-fuel combustion. Also the material may be well applicable to SOFC/SOEC composite electrodes where mixed conductivity is also desirable.

Manuscript submitted July 10, 2017; revised manuscript received September 21, 2017. Published October 4, 2017.

Dense ceramic oxygen transport membranes (OTMs) could potentially be applied for production of high purity oxygen for medical purposes, supply of oxygen in the steel industry, oxy-fuel combustion schemes, as well as in the cement and glass industries. Also, importantly, OTMs can beneficially be integrated with a biomass gasifier, allowing production of syngas (CO and H_2), which is a precursor for a variety of high value chemicals.[1]

Besides being applicable for OTMs,[2] acceptor doped-ceria has been intensively studied for use in a number of other applications e.g. solid oxide fuel cells (SOFCs),[3] solid oxide electrolysis cells (SOECs)[4] and for electrocatalysis.[5] In particular, acceptor doped ceria (e.g. CGO) is interesting owing to high oxide ion conductivity (0.12 Scm^{-1} for $Gd_{0.1}Ce_{0.9}O_{1.95-\delta}$ at 900°C[6]), appreciable electrocatalytic activity, high electronic conductivity under reducing conditions, and excellent chemical stability under harsh reducing and even corrosive gaseous conditions.[3,7] Kaiser et al.[8] reported that the oxygen permeation flux of a 27 μm asymmetric 10 at.% Gd-doped ceria-based membrane exceeds 10 ml cm^{-2} min^{-1} under a gradient of air/H_2 at 850°C,[9] which is promising for applications provided that sufficient lifetime can be achieved. However, the ambipolar conductivity of ceria is relatively low when only mildly reducing conditions are imposed because of the low electronic conductivity under these conditions (<1 × 10^{-3} Scm^{-1} at 900°C in air[10]). The low electronic conductivity also results in the slow oxygen surface exchange rate,[11,12] which further limits the achievable oxygen flux. To provide technologically relevant oxygen fluxes for high pO_2 applications, such as production of pure oxygen and in oxy-coal combustion conditions, the electronic conductivity of CGO needs to be enhanced preferably to a value close to that of the ionic conductivity so that ambipolar conductivity can be maximized.

Doping redox active elements is a feasible strategy to enhance the electronic conductivity of ceria.[13–18] Among rare earth elements, Praseodymium (Pr) and Terbium (Tb) show significant redox activity under mildly reducing conditions ($pO_2 = 1 \times 10^{-8}$−1 bar). Upon the reduction of Pr and Tb, electrons can migrate between the trivalent and tetravalent Pr/Tb, giving rise to an enhanced electronic conductivity. For instance, the *p*-type electronic conductivity of 3 at.% Pr-doped $Gd_{0.2}Ce_{0.8}O_{1.9-\delta}$ is enhanced by approximately 10 times relative to pure CGO in the temperature range from 600°C to 750°C.[13] The electronic conductivity of Tb and Pr dual-doped ceria can be modified by changing the ratio between the two dopants: higher relative amount of Pr yields higher electronic conductivity, but leads to larger chemical expansion.[16] Chatzichristodoulou et al.[16] and Bishop et al.[19] also found that doping Pr in ceria induces large chemical expansion, which will affect the thermomechanical stability of the material. It is thus of importance to examine the possible existence of an optimum amount of Pr in ceria that ensures satisfactory thermomechanical stability along with sufficient electronic conductivity.

When dissolved in the ceria lattice, Pr exists in two valence states.[16] Upon increasing pO_2 and decreasing temperature, the concentration of Pr^{4+} increases, accompanied by a decrease of oxygen vacancy concentration ($2Pr'_{Ce} + 1/2O_2 + V_O^{\bullet\bullet} = 2Pr^{\times}_{Ce} + O^{\times}_O$). In order to achieve, simultaneously, considerable oxygen vacancy and electron hole concentrations, various concentrations of Pr were doped in $Gd_{0.1}Ce_{0.9}O_{1.95-\delta}$ (partial Pr-substitution for Ce) and the effects were studied. Considerable oxygen vacancy concentration is expected in order to compensate the charge of the aliovalent dopants Gd'_{Ce} and Pr'_{Ce}. The influence of dopant concentration on the electronic and ionic conductivity was investigated using ion-blocking Hebb-Wagner polarization in conjunction with electrochemical impedance spectroscopy. Also effects on the achievable oxygen permeation fluxes were addressed to assess the potential of these materials for OTMs.

Theoretical Consideration

In $Pr_xGd_{0.1}Ce_{0.9-x}O_{1.95-\delta}$, oxygen vacancies are formed to compensate effectively negatively charged Gd^{3+}, Pr^{3+} and Ce^{3+} that partially substitute Ce^{4+}. Assuming ideal behavior for the reduction of Pr and Ce in the lattice (invariant values of reaction entropies and enthalpies),

*Electrochemical Society Member.
[z]E-mail: cheng_shiyang@foxmail.com; pvhe@dtu.dk

the expected defect reactions and mass action laws are:

$$Gd_2O_3 \overset{CeO_2}{\rightarrow} 2Gd'_{Ce} + V_O^{\bullet\bullet} + 3O_O^x \quad [1]$$

$$2\mathrm{Pr}_{Ce}^x + O_O^x \leftrightarrow 2\mathrm{Pr}'_{Ce} + V_O^{\bullet\bullet} + 1/2O_2\,(g) \quad [2]$$

$$K_{\mathrm{Pr}} = \exp\left(-\frac{\Delta H^0_{\mathrm{Pr}} - T\Delta S^0_{\mathrm{Pr}}}{RT}\right) = \frac{P_{O_2}^{1/2}\cdot\left[V_O^{\bullet\bullet}\right]\cdot\left[\mathrm{Pr}'_{Ce}\right]^2}{\left[O_O^x\right]\cdot\left[\mathrm{Pr}_{Ce}^x\right]^2} \quad [3]$$

$$2Ce_{Ce}^x + O_O^x \rightarrow 2Ce'_{Ce} + V_O^{\bullet\bullet} + 1/2O_2\,(g) \quad [4]$$

$$K_{Ce} = \exp\left(-\frac{\Delta H^0_{Ce} - T\Delta S^0_{Ce}}{RT}\right) = \frac{P_{O_2}^{1/2}\cdot\left[V_O^{\bullet\bullet}\right]\cdot\left[Ce'_{Ce}\right]^2}{\left[O_O^x\right]\cdot\left[Ce_{Ce}^x\right]^2} \quad [5]$$

Mass and site balances and electroneutrality requires:

$$\left[Ce'_{Ce}\right] + \left[\mathrm{Pr}'_{Ce}\right] + \left[Gd'_{Ce}\right] = 2\left[V_O^{\bullet\bullet}\right] \quad [6]$$

$$\left[Ce'_{Ce}\right] + \left[\mathrm{Pr}'_{Ce}\right] + \left[Gd'_{Ce}\right] + \left[Ce_{Ce}^x\right] + \left[\mathrm{Pr}_{Ce}^x\right] = 1 \quad [7]$$

$$\left[\mathrm{Pr}'_{Ce}\right] + \left[\mathrm{Pr}_{Ce}^x\right] = x \quad [8]$$

$$\left[V_O^{\bullet\bullet}\right] + \left[O_O^x\right] = 2 \quad [9]$$

$$\left[Gd'_{Ce}\right] = 0.1 \quad [10]$$

Under oxidizing conditions, where $[Ce'_{Ce}] \ll [Ce_{Ce}^x]$, the coexistence of $\mathrm{Pr}'_{\mathrm{Pr}}$ and $\mathrm{Pr}^x_{\mathrm{Pr}}$ leads to p-type electronic conductivity.[20,21] Assuming the reduction of cerium under oxidizing conditions to be negligible, the variation in oxygen non-stoichiometry (δ) (arising from redox of Pr only) can be calculated by the following equation:

$$K_{\mathrm{Pr}} = \frac{p_{O_2}^{1/2}\delta(2\delta)^2}{(1.95-\delta)(x-2\delta)^2} \quad [11]$$

The equilibrium constant for the reduction reaction of Pr can be obtained by fitting Eq. 11 to oxygen nonstoichiometry vs. pO_2 –data (at high pO_2, $pO_2 > 1 \times 10^{-4}$ bar), as will be shown in 4.4.

Experimental

Sample preparation and phase identification.—The specimens in this work were synthesized by solid state reaction. Stoichiometric amounts of precursors of $Ce(NO_3)_3 \cdot 6H_2O$ (Sigma Aldrich 99.99%), Gd_2O_3 (Alfa Aesar 99.9%), Pr_6O_{11} (Alfa Aesar 99.9%) and Co_3O_4 (Alfa Aesar 99.9%, for cobalt containing samples) were mixed by ball milling in ethanol for 24 hours. The resultant mixed powders were dried at 80°C for 10 hours and subsequently calcined at 1000°C for 5 hours. The calcined powders were then uniaxially cold pressed at 400 MPa followed by isostatic pressing at 600 MPa. Cobalt-containing and cobalt-free pellets were sintered at 1200°C and 1600°C for 10 hours, respectively.

The crystal structures of the material (crushed sintered pellets) were characterized by X-ray powder diffraction (XRD). The XRD patterns were obtained with Cu Kα radiation using a Bruker Robot operating in Bragg-Brentano geometry in the 2θ range from 20° to 90°. The obtained XRD patterns were indexed with the ICCD (International Centre for Diffraction Data) database by means of the software named DIFFRAC plus. Scanning electron microscopy (SEM) was carried out on a FE-SEM Zeiss Supra 35 electron microscope using an acceleration voltage of 15 kV.

Thermogravimetry.—Thermogravimetric analysis (TGA) was performed using a Netzsch STA 409CD thermogravimeter and a Netzsch TG 439 thermal balance. The samples were prepared by uniaxially pressing the powder into pellets at a pressure of 400 MPa in a capillary die (ø = 0.5 cm). Porous samples were obtained by sintering the green sample at 1000°C for 3 hours at heating and cooling rate of 2°C min^{-1}. Buoyancy effects were corrected for by measuring the mass change of an Al_2O_3 powder sample with the same volume under the same conditions.

Dilatometry.—Dilatometry measurements were performed using a differential contact dilatometer (DIL 402CD, NETZSCH GmbH, Germany). The samples were rectangular bars with a dimension of $1 \times 1 \times 10$ mm^3. An Al_2O_3 reference with a similar dimension was tested simultaneously with the sample. The heating rate was kept at 3°C min^{-1} to a final temperature of 1000°C. All the measurements were conducted in air with a total gas flow of 50 ml min^{-1} controlled by a mass flow controller.

Impedance spectroscopy.—The total conductivity of each specimen was measured by Electrical Impedance Spectroscopy (EIS). Prior to the electrical measurements, symmetric $(La_{0.6}Sr_{0.4})_{0.99}CoO_{3-\delta}$ (LSC) electrodes were screen printed on both sides of a 1-mm thick polished pellet (ø = 10 mm), followed by sintering at 1000°C for 2 hours to obtain good adhesions between the specimen and the electrodes. The LSC electrodes were then covered with Pt layers (current collector) by hand painting to eliminate any contact resistance. EIS was carried out in the temperature range from 600°C to 900°C using a Solartron 1260 impedance spectrometer within the frequency range from 3 MHz down to 0.1 Hz under a fixed fluctuation voltage of 20 mV. Impedance spectra were plotted and fitted by the software package "Z-view" and "Z-plot". The specimens were placed in a closed alumina chamber in which oxygen partial pressure was varied and monitored by controlling the flow of air and nitrogen by mass flow controllers. The oxygen partial pressure around the samples was measured by a zirconia-based sensor placed in close proximately to the sample.

Microelectrode ion-blocking Hebb-Wagner polarization measurements.—The electronic conductivity of each sample was measured by means of a microelectrode ion- blocking Hebb-Wagner polarization method. Prior to the measurements, 1-mm thick dense circular samples (ø = 10 mm) were polished by SiC #300 sand papers, followed by further polishing using SiC #1000 and #1600 sand papers. The Hebb-Wagner measurement cell is schematically illustrated in Fig. 1. Similar setups have been used in a number of papers in the past.[13,22–25] A Pt microelectrode with a contact radius of 100–500 μm was placed on the sample under an external load. The periphery of the Pt microelectrode was sealed with a customized glass sealant (MgO/sodium aluminosilicate glass composites, 30/70 vol. %). The Hebb-Wagner cell was sandwiched with two Pt current collectors. The whole cell was finally placed inside a furnace in which the oxygen partial pressure was maintained at 0.21 atm by flowing 100 ml min^{-1} of air. The cell was initially heated up to 950°C at the rate of 1°C min^{-1} to soften the glass sealant, followed by cooling down to 750°C at the same rate to achieve a gastight solidified glass. The polarization measurement was then performed by stepwise varying voltage in 25 mV steps in the range from −800 to 200 mV. The steady state was achieved by dwelling for 12 minutes (more than 100 times the theoretical time needed to reach the steady state) in each step. The oxygen partial pressure in the vicinity of the microelectrode can be calculated by the Nernst equation:

$$a_{O_2,micro} = a_{O_2,ref}\exp\left(\frac{4FV}{RT}\right) \quad [12]$$

where $a_{O_2,micro}$ and $a_{O_2,ref}$ is the oxygen activity near the microelectrode and reference electrode, respectively. V is the polarization voltage applied on the microelectrode relative to the reference/counter electrode. The sum of electron and electron hole conductivity in the vicinity of the ion-blocking microelectrode can, under a set of assumptions,[13,24,26] be calculated in terms of the derivative of the

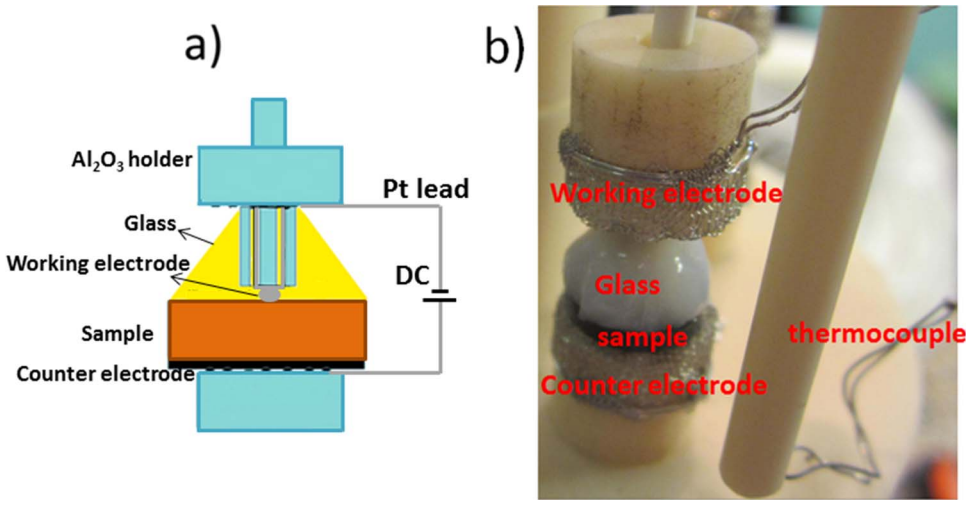

Figure 1. (a) Schematic illustration and (b) image of the Hebb-Wagner polarization setup.

steady state I-V curve:

$$\frac{\partial I}{\partial V} = 2\pi r_c(\sigma_e + \sigma_h) \quad [13]$$

where r_c is the radius of the spherical microelectrode. If the micron-sized contact is circular rather than spherical, the factor $2\pi r_c$ is replaced by $4r_c$.[24]

Oxygen permeation measurements.—Oxygen permeation measurements were performed in the customized test configuration displayed in Fig. 2. Before the flux measurements, circular samples (ø ≈12 mm) were polished by SiC #500 sand papers to achieve a thickness of approximately 1 mm. To mitigate the effect of slow surface exchange, a highly porous circular $La_{0.6}Sr_{0.4}CoO_{3-\delta}$ (LSC)-based catalytic layer (ø ≈5 mm) was applied on the dense samples by screen printing with a LSC-based ink. The as-prepared catalytic layers were then calcined at 900°C for 1 hour to obtain good adhesion with the membrane surface. The area covered with the catalytic layer is ~0.8 cm^2.

The samples were sealed between two alumina tubes using a 30/70 vol.% mixture of a MgO and sodium aluminosilicate glass. The feed side tube below the membrane was supplied with gas from the feed side manifold, which featured a feed gas inlet and outlet. Similarly, the permeate side of the membrane was purged with gas from a "permeate side" manifold. The feed side was flushed with air with a constant flow rate of 100 Nml min^{-1}, and the permeate side was flushed at various flow rates of N_2 (from 30 to 300 Nml min^{-1}). All gas flows were measured by mass flow controllers. The net oxygen permeation flux can be deduced from the pO_2 difference between inlet and outlet gases. The pO_2 was monitored by two customized YSZ-based oxygen sensors. The total leak in the system was assessed by means of a mass flow meter on the permeate stream. When perfect sealing is achieved, the outlet gas flow rate is equivalent to the inlet flow plus the flow of the permeated oxygen. If there are leaks in the membrane or pinholes or cracks in the glass encapsulation, the flow rate of the outlet gas will be lower than that of the inlet gas. Typically, when a significant leak is observed during the permeation measurement, a thermally activated increase in oxygen flux is not observed. In the data reported here,

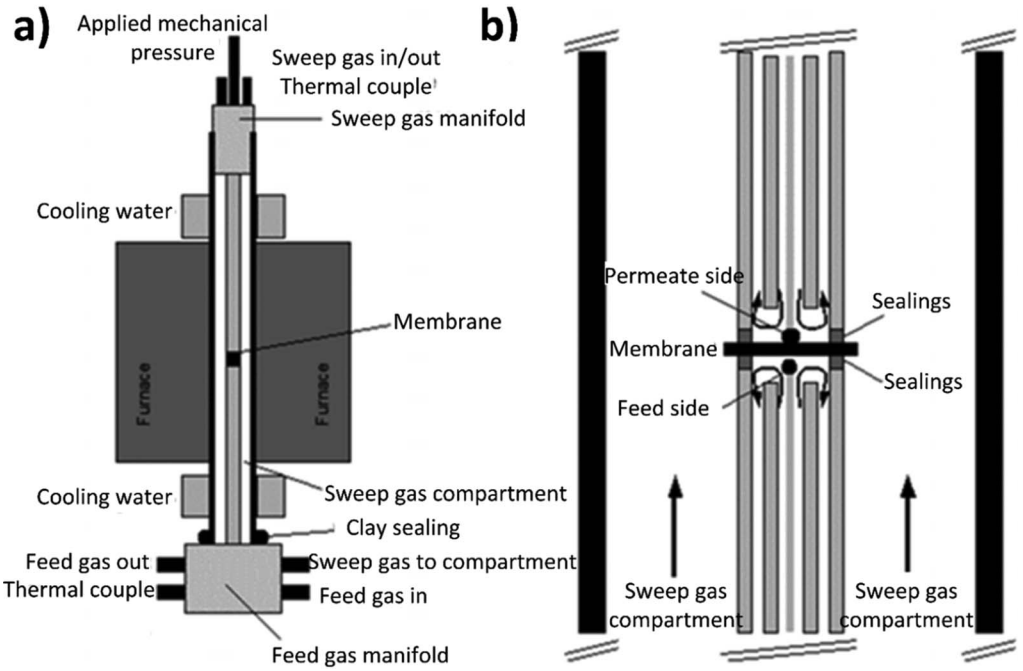

Figure 2. (a) Schematic illustration of the membrane test rig. (b) Local enlargement of the heated part of the membrane test rig.

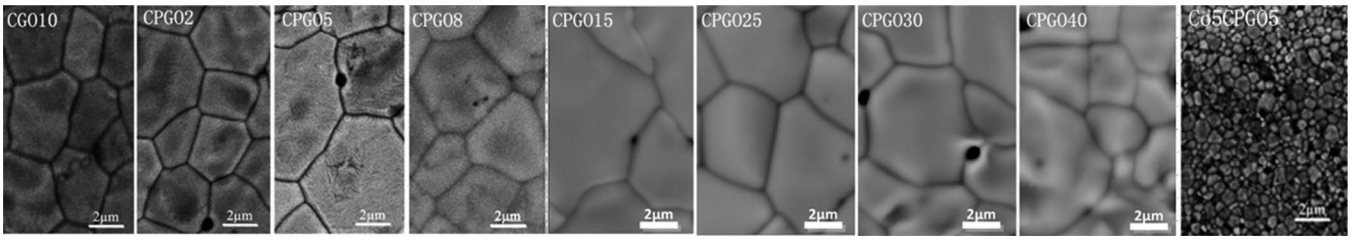

Figure 3. SEM micrographs (Back-scattered electrons) of polished and thermally etched surfaces of the investigated samples. (scale bar = 2 μm).

Table I. Sintering temperature, density and grain size of pure and Pr-doped CGO.

Abbreviated name	Composition	T_s/°C	Theoretical density/gcm^{-3}	Measured geometrical density/g cm^{-3}	Relative density%	d_g/μm
CGO	$Gd_{0.1}Ce_{0.9}O_{1.95}$	1600	7.20	7.10	98.6	3.0 ± 1.0
CPGO2	$Pr_{0.02}Gd_{0.1}Ce_{0.88}O_{1.95-\delta}$	1600	7.18	6.90	96.1	4.0 ± 1.0
CPGO5	$Pr_{0.05}Gd_{0.1}Ce_{0.85}O_{1.95-\delta}$	1600	7.24	6.95	96.0	5.0 ± 1.0
Co2CPGO5	$Co_{0.02}Pr_{0.05}Gd_{0.1}Ce_{0.85}O_{1.95-}$	1200	7.24	7.02	97.0	0.2–0.5
Co5CPGO5	$Co_{0.05}Pr_{0.05}Gd_{0.1}Ce_{0.85}O_{1.95\delta}$	1200	7.25	7.05	97.2	0.2–0.5
CPGO8	$Pr_{0.08}Gd_{0.1}Ce_{0.82}O_{1.95-\delta}$	1600	7.22	7.10	98.3	4.0 ± 1.0
CPGO15	$Pr_{0.15}Gd_{0.1}Ce_{0.75}O_{1.95-\delta}$	1600	7.13	6.60	92.6	4.0 ± 1.0
CPGO25	$Pr_{0.25}Gd_{0.1}Ce_{0.65}O_{1.95-\delta}$	1600	7.03	6.50	92.5	5.0 ± 1.0
CPGO30	$Pr_{0.3}Gd_{0.1}Ce_{0.6}O_{1.95-\delta}$	1600	6.92	6.20	89.6	6.0 ± 1.0
CPGO40	$Pr_{0.4}Gd_{0.1}Ce_{0.5}O_{1.95-\delta}$	1600	6.70	6.30	94.0	6.0 ± 1.0

the inlet and outlet flows were identical (within 1% uncertainty) and a thermal activated oxygen permeation flux was observed, indicating close to perfect sealing. The maximum leak originating from pinholes in the sealant and from other sources of oxygen in the permeate flow through the membrane is estimated to be lower than 5% of the measured oxygen flux at low temperature (600°C). Below 600°C a large leak appeared as a result of sealant failure driven by thermal expansion mismatch between membrane and manifold tubes.

Results

Sintering.—Fig. 3 displays the microstructure of thermally etched samples of different composition. Table I summarizes the specific composition, sintering temperature (Ts), theoretical density, measured density, relative density and average grain size of the specimens analyzed. The average grain size of the cobalt oxide free samples sintered at 1600°C lies in the range from 2 to 5 μm, and shows a slightly increasing tendency with increasing Pr content. The cobalt oxide containing samples sintered at 1200°C are completely dense with relatively small average grain size (200–500 nm). This elucidates that cobalt oxide serves as an effective sintering aid in doped ceria, which is well in line with literature.[27]

X-ray diffraction.—XRD patterns of crushed dense pellets of $Pr_xGd_{0.1}Ce_{0.9-x}O_{1.95-\delta}$ (x = 0.02, 0.05, 0.08, 0.15, 0.25, 0.3 and 0.4) and $Co_xPr_{0.05}Gd_{0.1}Ces_{0.85}O_{1.95-\delta}$ (x = 0.02 and 0.05) are shown in Fig. 4. Zero shifts were compensated for using an internal standard (LaB_6 powder). No significant shift of the (111) reflection was detected, indicative of an insignificant influence of the addition of the dopant on the lattice parameter. No indication of secondary phases originating from side reactions or precipitation of insolvable dopants can be detected within the resolution limit of the XRD, indicating that the solubility limit of Pr in CGO is more than 40 at.%, which is in accordance with the solubility limit of 70 at.% reported by Taksu et al.[28] for partial Pr-substitution for cerium in $Pr_xCe_{1-x}O_{2-0.5x}$ at 1400°C. Co_3O_4 and CoO phases could not be indexed from the diffractograms of $Co_xPr_{0.05}Gd_{0.1}Ce_{0.85}O_{1.95-\delta}$ (x = 0.05). Due to the high temperature (1200°C) used to sinter the cobalt-containing samples, any cobalt oxide not dissolved in the fluorite phase may likely react with trivalent Gd, Pr cations, forming small amounts of $GdCoO_3$ or $PrCoO_3$ phases

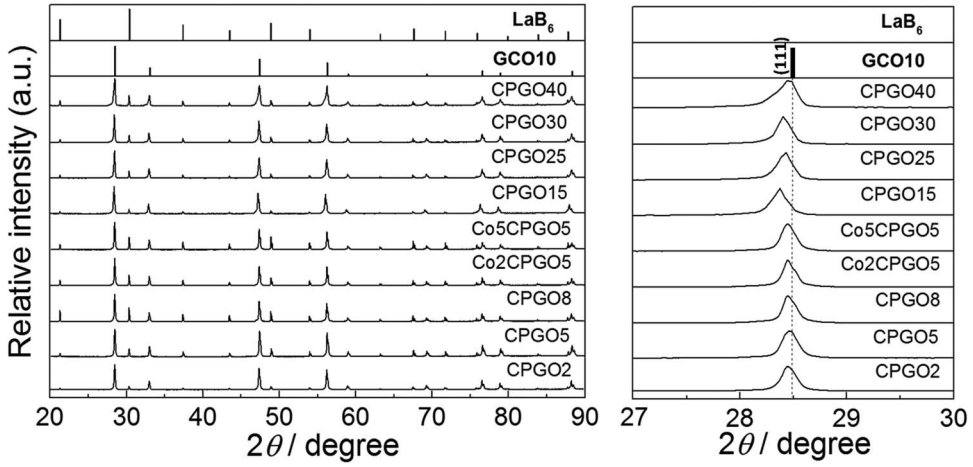

Figure 4. Powder X-ray diffraction patterns of $Pr_xGd_{0.1}Ce_{0.9-x}O_{1.95-\delta}$ (x = 0.02, 0.05, 0.08, 0.15, 0.25, 0.3 and 0.4) and $Co_xPr_{0.05}Gd_{0.1}Ce_{0.85}O_{1.95-\delta}$ (x = 0.02 and 0.05). Inset: zoom corresponding to the (111) reflection in the 2θ range from 27 to 30 degree.

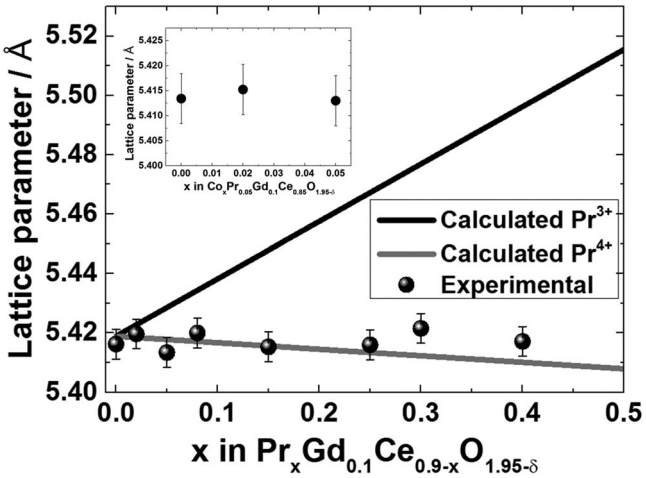

Figure 5. Experimental and calculated lattice parameters vs. Pr concentration. Inset: lattice parameter vs. x in $Co_xPr_{0.05}Gd_{0.1}Ce_{0.9}O_{1.95-\delta}$.

for which the highest intensity peaks ($2\theta \approx 32^\circ$, $PrCoO_3$:PDF#25-1069 and $GdCoO_3$:PDF#25-1057) would be "hidden" by the peak of the (200) crystal planes from the main phase.

Lattice parameter and microstructure.—The lattice parameter obtained from XRD is shown in Fig. 5 along with calculated lattice parameters obtained by Kim's empirical formula[29]

$$a = 0.5413 + \sum_k (0.022\Delta r_k + 0.00015\Delta z_k)m_k \qquad [14]$$

where a is the unit cell parameter of the fluorite oxide at room temperature, ($\Delta r_k = r_k - r_h$) is the difference in ionic radius of the kth dopant (r_k) and the host cation (r_h) in eight-fold coordination from Shannon's compilation,[30] ($\Delta z_k = z_k - z_h$) is the valence difference between dopant and host, and m_k is the mole fraction of the kth dopant in the form of PrO_x ($x = 1.5/2$).

As displayed in Fig. 5, the experimentally observed lattice parameter lies closer to the calculated values for Pr being tetravalent (Pr^{4+}) in the materials than when assuming Pr^{3+}. McCullough reported that praseodymium is readily oxidized to Pr^{4+} in the presence of Ce^{4+}.[31] This suggests that the concentration of tetravalent Pr prevails at room temperature in the Pr-doped CGO (slow cooling in air). Due to the similar ionic radii between Pr^{4+} (CN = VIII 0.96 Å[30]) and Ce^{4+} (CN = VIII 0.97 Å[30]), the lattice parameter does not vary significantly with increasing dopant concentration, which is similar to the trend observed in purely Pr-doped ceria.[32] The lattice parameter of the Co-containing samples does not deviate from the Co-free comparable specimens. Lewis et al.[33] reported a similar result that the lattice constant of CGO is not influenced by the addition of cobalt oxide because the cobalt is effectively insoluble in the CGO lattice.

Table II. The thermodynamic parameters for the reduction of Pr in CPGO15, CPGO25, CPGO30 and CPGO40.

Sample	ΔH_{Pr} /kJ mol^{-1}	ΔS_{Pr} / J K^{-1} mol^{-1}	Ref.
CPGO8	200 ± 34	158 ± 34	This work
CPGO15	204 ± 25	156 ± 24	This work
CPGO25	132 ± 15	108 ± 14	This work
CPGO30	130 ± 14	108 ± 14	This work
CPGO40	112 ± 10	93 ± 12	This work
CPO10	137	n/a	35
CPO20	140	83	20

Oxygen nonstoichiometry.—Fig. 6 displays the oxygen nonstoichiometry data of the samples along with the best least square fit curves ($0.90 < R^2 < 0.99$) using the ideal defect model (Eq. 11). In the investigated pO_2 regime (blue regime) the oxygen nonstoichiometry (δ) increases with decreasing oxygen partial pressure until it reaches a plateau (at $\delta = x/2$), where all the Pr is trivalent. The equilibrium constants (K_{Pr}) at each temperature were obtained from the fit of the defect model to the data. The equilibrium enthalpy and entropy were obtained from the slope and intercept of the linear fit to the data of $-\ln(K_{Pr})$ vs. $1/T$ according to the equation:

$$-\ln K_{Pr} = \frac{\Delta H_{Pr}}{RT} - \frac{\Delta S_{Pr}}{R} \qquad [15]$$

The thermodynamic parameters thus deduced for each composition are summarized in Table II. It is noteworthy that the enthalpy of reduction of Pr decreases with increasing Pr concentration, indicating a more facile reduction of Pr and release of oxygen with increasing Pr concentration or oxygen nonstoichiometry. Chatzichristodoulou et al.[16] also found that reduction is facilitated with increasing oxygen nonstoichiometry in Pr and Tb co-doped ceria. Stefanik et al.[34] also pointed out that the reduction enthalpy of Pr decreases with increasing Pr concentration, indicating higher Pr concentration gives rise to higher reducibility, which is consistent with the general trend observed in th is work.

Thermal expansion.—Thermal expansion curves of $Pr_xGd_{0.1}Ce_{0.9-x}O_{1.95-\delta}$ measured on cooling the samples from 900°C to room temperature in air are shown in Fig. 7a. Below 400°C, all the samples show linear expansion. However, the curves display a non-linear behavior with an inflection point in the range from 500°C to 600°C, particularly for the samples with 15 at.% Pr or more. It is evident that Pr-doped CGO follows a similar tendency as Pr doped ceria where the strain increases with increasing Pr concentration in the specimen. The increased and highly non-linear apparent

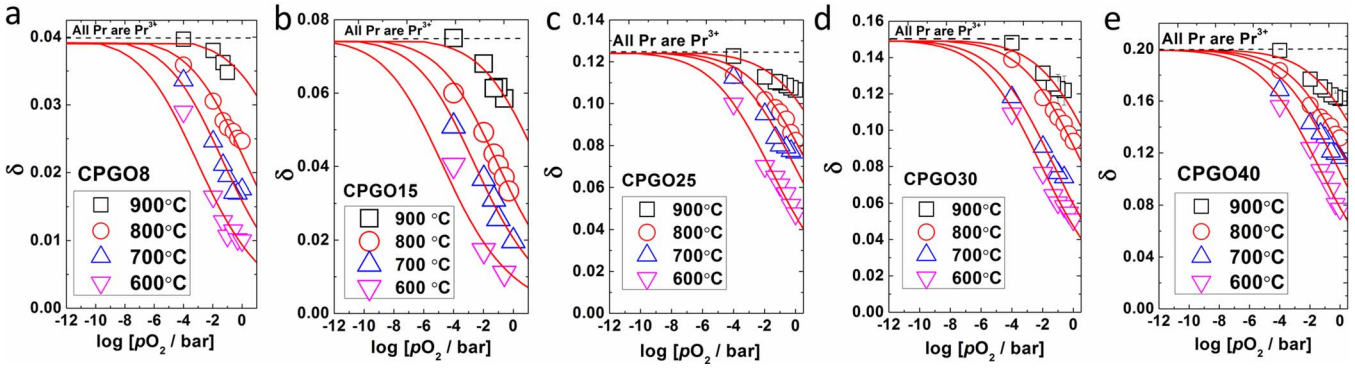

Figure 6. Fit of the ideal defect model to the oxygen nonstoichiometry data of (a) CPGO8, (b) CPGO15, (c) CPGO25, (d) CPGO30 and (e) CPGO40 measured by TGA.

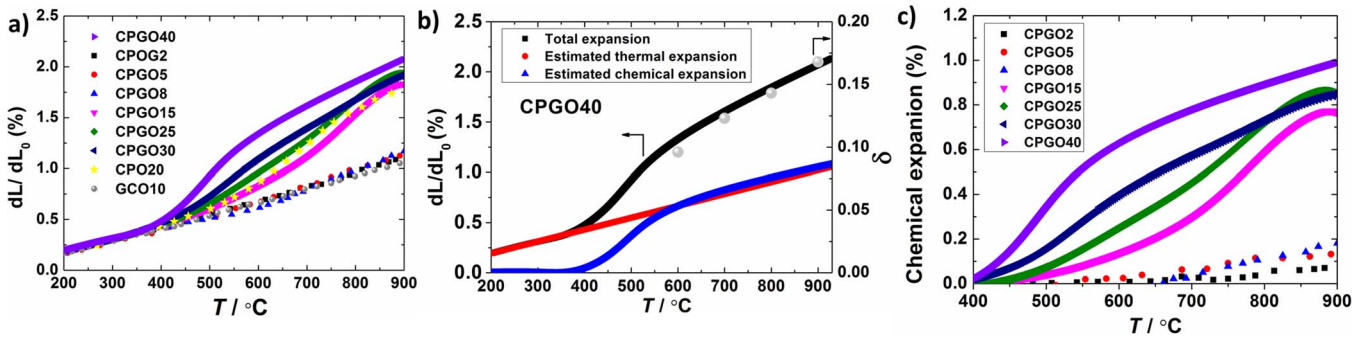

Figure 7. (a) Thermal expansion curves for $Pr_xGd_{0.1}Ce_{0.9-x}O_{1.95-\delta}$ in air. The strain of CPO20 is the data taken from Ref. 16 (b) Temperature dependence of oxygen nonstoichiometry, thermal expansion and estimated chemical expansion curve of CPGO40. c) Estimated chemical expansion of CPGO as a function of temperature.

TEC in Pr-doped ceria is primarily ascribed to the chemical strain originating from the combination of slight contraction of the unit cell upon formation of oxygen vacancies and expansion of the unit cell upon partial reduction of Pr.[16,36] The total expansion (the measured quantity) is the sum of the thermal and the chemical expansion (stoichiometric expansion[37]), which can be written:

$$\varepsilon = \alpha \Delta T + \beta \Delta \delta \qquad [16]$$

where α is the thermal expansion coefficient (TEC), and β is the stoichiometric expansion coefficient.[37] Assuming a constant thermal and stoichiometric expansion coefficient[37] at a given oxygen partial pressure, the non-linear total expansion curve can be fitted by a linear thermal expansion curve and a nonlinear chemical expansion curve (Fig. 7b). Values of the thermal expansion and chemical stoichiometric expansion coefficients deduced from this type of fitting are listed in Table III. The chemical expansion coefficient is observed to decrease with increasing dopant concentration. For samples doped with similar Pr concentration ($Pr_{0.2}Ce_{0.8}O_{1.9-\delta}$ vs. CPGO25), the chemical expansion coefficients are very close. (0.084 mol^{-1} for $Pr_{0.2}Ce_{0.8}O_{1.9}$[16] and 0.08 mol^{-1} for CPGO25). It should be noted that Eq. 16 applies in general to small perturbations; β is best determined at constant temperature with a change in δ driven by varying pO_2, and α should be determined at fixed δ. We did not conduct such differential measurements (isothermal dilatometry). In the analysis presented, leading to estimates of β (Table III), one assumes that the α value determined at low temperature (where changes δ in are small) is constant in the whole temperature range.

Electronic conductivity (blocking electrode measurement).—The contact area of the Pt microelectrode was determined using Newman's formula[38]

$$r_c = \frac{1}{4R_s\sigma} \qquad [17]$$

where r_c is the radius of the micro-electrode, R_s is the serial resistance found from the intercept with the real axis at the high frequency of the impedance spectra and σ is the conductivity of the sample. The contact radius thus determined was typically between 100 μm and 500 μm, in good agreement with Ref. 24 where similar conditions were applied. The contact radius evaluated by impedance spectroscopy was as expected not sensitive to the temperature or oxygen partial pressure.

The plots of the steady state current density of CPGO8 measured in the blocking electrode geometry versus the potential at 700°C, 800°C and 900°C are presented in Fig. 8. A current plateau in the range of −0.4–0 V is observed. Excellent coincidence of the branches recorded in the negative and positive polarization direction upon repeated cycles indicate that any hysteresis arising from creep of the Pt micro-electrode and/or sluggish equilibrium between the redox of Pr^{3+} and Pr^{4+} is negligible, and accordingly confirms that the I-V curves are obtained in the steady state.

Total and electronic conductivity versus pO_2.—The oxygen activity dependence of the partial electronic and total conductivity of each sample is presented in Fig. 9. The electronic conductivity of CGO measured in this work agrees well with the electronic conductivity of

Table III. Integrated thermal and expansion chemical expansion coefficients (200–900°C).

Abbreviated name	α_{int}/K^{-1}	α_{therm}/K^{-1}	β/mol^{-1} (600–900°C)
CGO	12.5×10^{-6}	12.5×10^{-6}	n/a
CPGO2	13.2×10^{-6}	12.5×10^{-6}	n/a
CPGO5	13.8×10^{-6}	12.5×10^{-6}	n/a
CPGO8	14.0×10^{-6}	12.5×10^{-6}	0.05
CPGO15	21.5×10^{-6}	12.5×10^{-6}	0.13
CPGO25	23.4×10^{-6}	12.5×10^{-6}	0.08
CPGO30	24.0×10^{-6}	12.5×10^{-6}	0.07
CPGO40	26.5×10^{-6}	12.5×10^{-6}	0.06
$Pr_{0.2}Ce_{0.8}O_{1.9-\delta}$[16]	22.7×10^{-6}	n/a	0.08
$Tb_{0.2}Ce_{0.8}O_{1.9-\delta}$[16]	18.2×10^{-6}	n/a	0.09

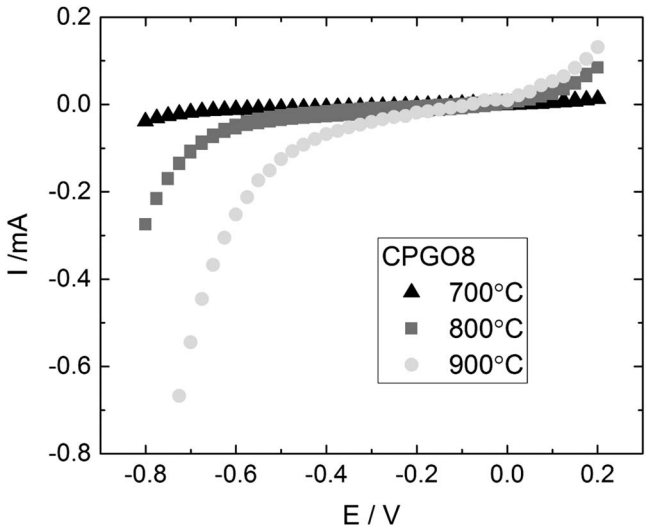

Figure 8. Steady state current voltage polarization curve at 700°C, 800°C and 900°C using air at the reference Pt electrode.

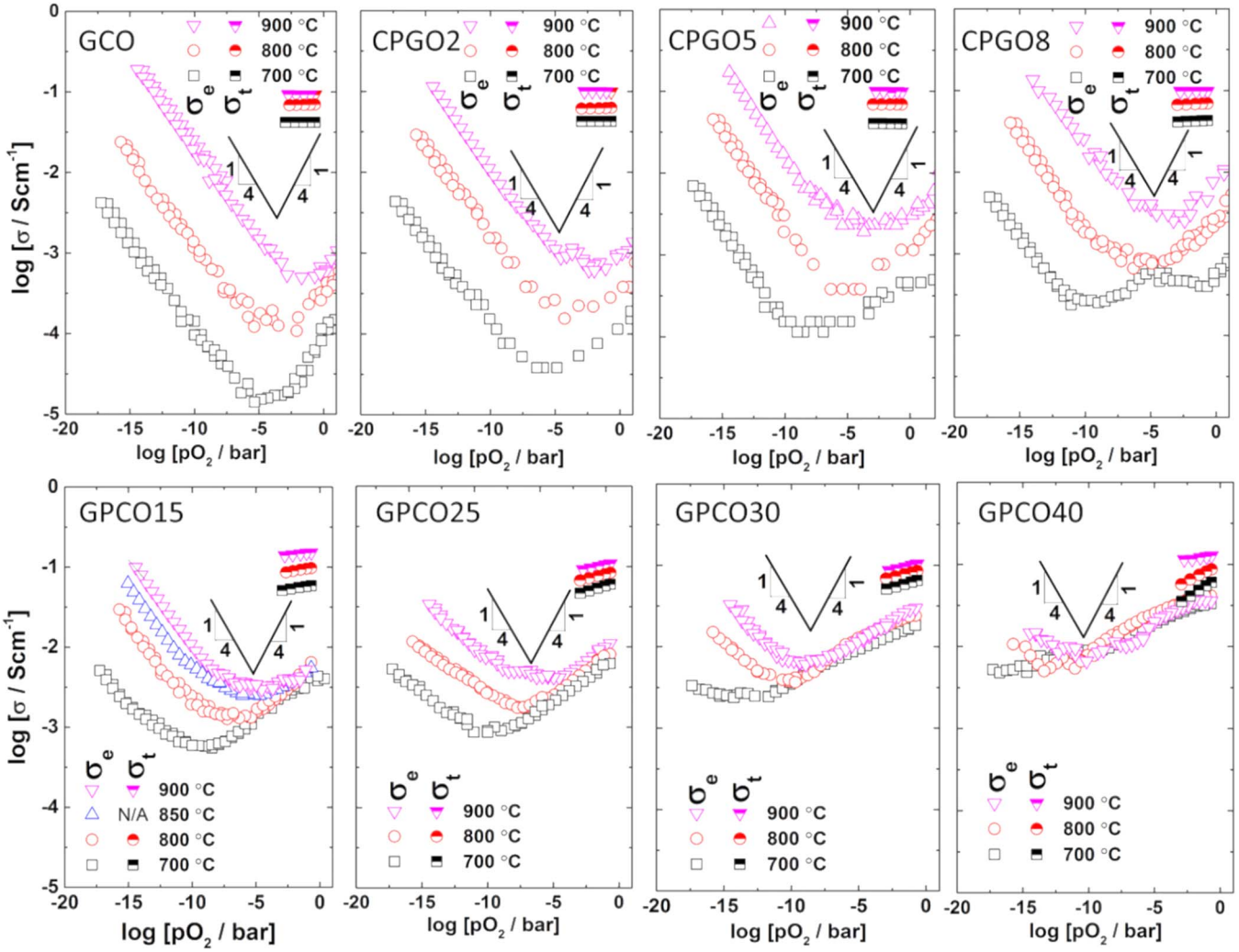

Figure 9. Logarithm of electronic (open symbols) and total conductivity (half filled) of $Pr_xGd_{0.1}Ce_{0.9-x}O_{1.95-\delta}$ (x = 0, 2, 5, 8, 15, 25, 30 and 40) versus log pO_2 at 900°C, 800°C and 700°C.

CGO reported by Chatzichristodoulou et al.[24] In general, the electronic conductivity of CPGO is dominated by n-type and p-type under low and high oxygen partial pressures, respectively. The minimum point at intermediate pO_2 corresponds to the transition from n-type to p-type conductivity. It is noteworthy that the minimum point shifts toward lower oxygen partial pressure with increasing Pr concentration.

In contrast to the electronic conductivity of CGO which follows a typical relationship of $\sigma_t = \sigma_n^0 pO_2^{-\frac{1}{4}} + \sigma_p^0 pO_2^{\frac{1}{4}}$, the electronic conductivity of CPGO possesses a more varied pO_2 dependency. The slope of the n-type electronic conductivity of slightly doped samples (CPGO2, CPGO5, CPGO8 and CPGO15) at low pO_2 approaches $-\frac{1}{4}$, whereas for the heavily doped samples (CPGO25, CPGO30 and CPGO40) the slope is depressed especially at low temperature.

Under oxidizing conditions, the slopes vary within the range from 1/4 to 1/8, in agreement with Ref. 13. Evidently, the p-type electronic conductivity strongly increases with increasing Pr concentration. In particular for CPGO40, the p-type electronic conductivity is higher than that of CGO by two orders of magnitude at 700°C. The observed enhancement of p-type conductivity upon Pr substitution is in line with previous literature.[13,16,39,40] It is also seen that the electronic conductivity becomes insensitive to the temperature for these heavily doped samples (>15 at.%), which coincides with previous findings by Chatzichristodoulou et al.[24] and Schmale et al.[25] This can be explained by the decreased concentration of Pr_{Ce}^{x} at elevated temperature which counteracts the increased mobility of the electron holes.[24]

The total conductivity is insensitive to the change of oxygen partial pressure in the range from 1×10^{-5} bar to 0.21 bar for Pr substitutions lower than 8 at.% whilst it shows detectable pO_2-dependence for Pr concentrations larger than 15 at.%. The pO_2-dependence becomes more pronounced with increasing Pr concentration because the electronic conductivity is sufficient to influence the total conductivity and the ionic conductivity decreases with decreasing pO_2 (as shown in Fig. 10).

In Fig. 10, the oxide ion conductivities were obtained by subtracting the electronic conductivities from the total conductivities (see Fig. 9). It can be observed that the oxide ion conductivity is invariant over the full pO_2 range for the samples doped with less than 15 at. % Pr but steadily decreases with decreasing pO_2 for the more heavily doped samples (>15 at. % Pr). As pO_2 decreases, the concentration of acceptor dopants increases because of the increasing $Pr_{Ce}^{/}$ concentration. Oxygen vacancy concentration accordingly increases to counterbalance the increased charge of acceptor dopants. The unchanged (CGO, CPGO2, CPGO5 and CPGO8) or decreased conductivity (CPGO15, CPGO25, CPGO30 and CPGO40) with decreasing pO_2 must be ascribed to a decreasing oxide ion mobility with increasing oxygen vacancy concentration and increasing concentration of Pr^{3+}. One does, in terms of ionic conductivity not benefit from doping beyond the 10 at.% Gd. This is well in line with literature on optimal conductivity in acceptor doped ceria which typically points to a maximum in ionic conductivity at doping levels between 10 and 20%.[41] The maximum

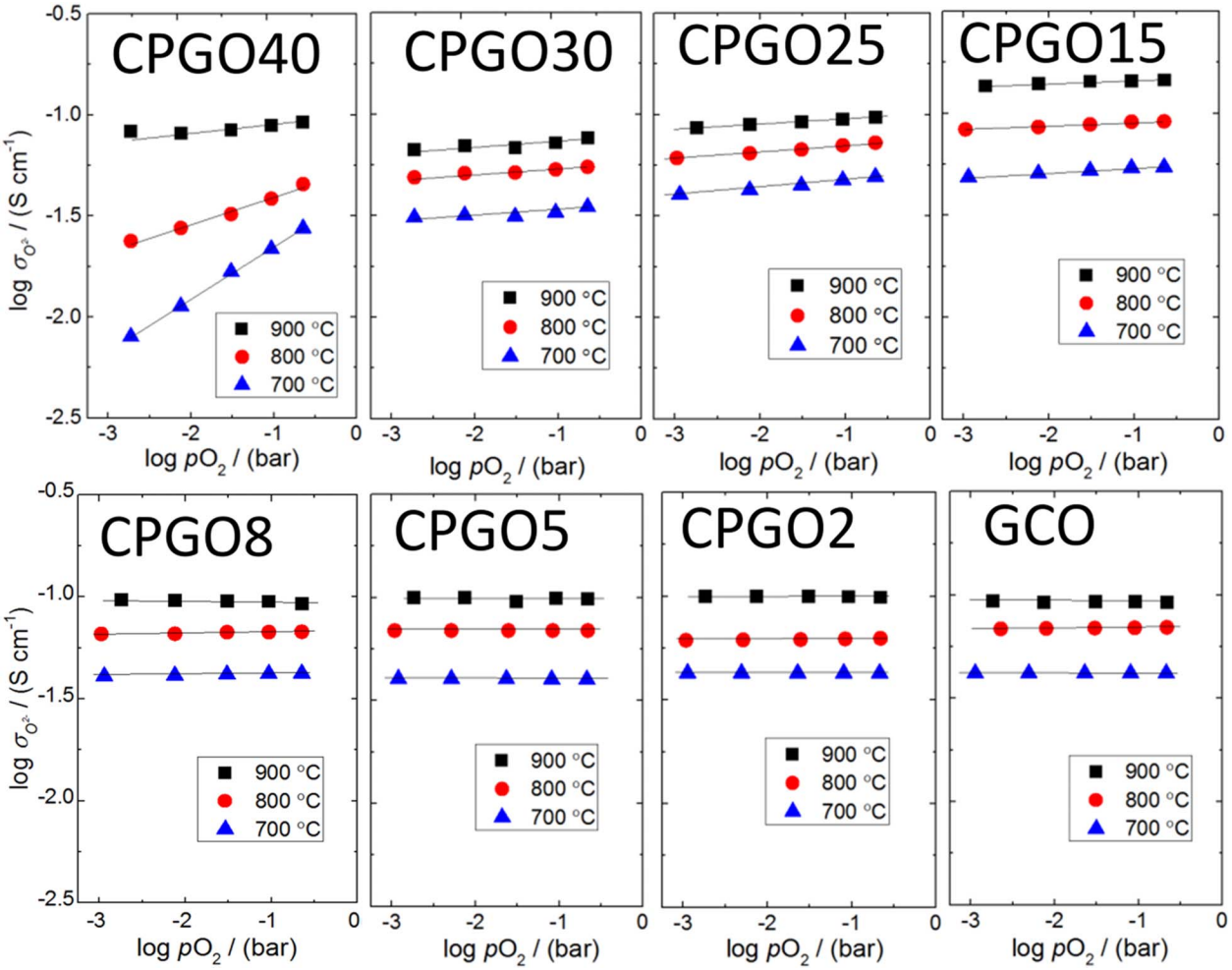

Figure 10. Logarithm of oxide ion conductivity versus log pO_2 for each composition. The lines were obtained by linear fitting to the data.

ionic conductivity in this doping regime is due to the trade off between the increased oxygen vacancy concentration and the development of deep vacancy association induced by electrostatic interaction.[3]

Calculated and measured oxygen permeation fluxes.—Fig. 11 displays the calculated and measured oxygen flux for CPGO5, Co5CPGO5 and CGO as a function of temperature under a fixed oxygen partial pressure difference ($\ln(pO_2'/pO_2'') = 7$). All samples in the flux measurements were coated on both sides with porous LSC layers (c.f. Oxygen permeation measurements section). The calculated fluxes were obtained from Wagner's equation using the measured electronic and ionic conductivity (see Figs. 9 and 10). It is noteworthy that the calculated flux is consistent with the measured flux. This indicates that the measured oxygen flux is limited by bulk ambipolar diffusion in the 1-mm thick pellet investigated rather than surface exchange. Another noticeable feature is that the oxygen flux of CPGO5 is higher than that of CGO by a factor of five at 900°C. It has previously been reported that cobalt oxide containing ceria based membranes show enhanced oxygen flux compared to the corresponding cobalt oxide free membrane because percolating cobalt oxide forms along the grain boundaries enhancing electronic conductivity without influencing the ionic conductivity.[17,42,43] The enhanced oxygen flux is reported to be due to the enhanced electronic conductivity. However, we did not observe enhanced flux for the cobalt-containing sample, instead the opposite trend was observed. The slightly decreased oxygen flux in cobalt oxide containing samples in this work may be due to the formation of discrete CoO_x-rich segregations at the grain boundaries resulting from the high sintering temperature (1200°C) instead of forming a continuous percolating network as found in other studies.[17,42,43]

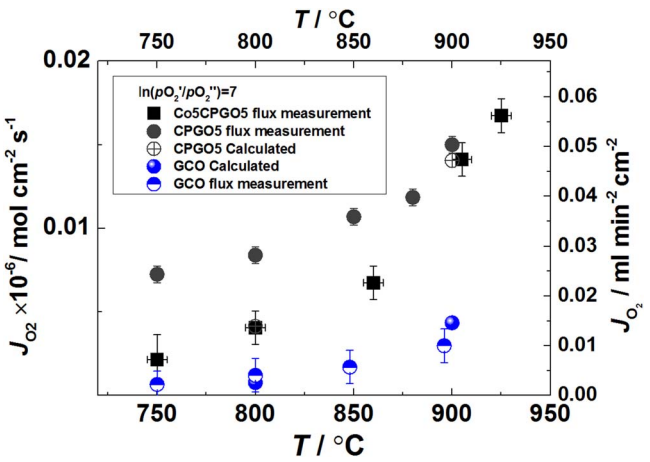

Figure 11. Calculated and measured oxygen permeation flux for CGO, CPGO5 and Co5CPGO5.

Discussion

Electronic conductivity under oxidizing conditions.—Praseodymium oxides (PrO_x) exist in variable compositions (x in the range from 1.5 to 2) at elevated temperatures where the valence

state of Pr thus varies between Pr^{3+} and Pr^{4+}. As the reduction of Pr occurs, the electrical conductivity of PrO_x significantly increases, up to a value of 1.4 Scm^{-1} at 850°C.[44] The electrical conductivity of PrO_x at high temperature is assigned to electronic conductivity, which originates from electron hopping between mixed-valence Pr^{3+}/Pr^{4+} cations present in the lattice. Unlike PrO_x, Gd-doped ceria is an oxide ion conductor with negligible p-type electronic conductivity under oxidizing condition. As observed (Figs. 8 and 9), a combination of PrO_x and Gd-doped ceria; making a Pr/Gd co-doped ceria solid solution gives rise to mixed ionic-electronic conductivity.

The mechanism for the mixed ionic-electronic conductivity of Pr in ceria has been rationalized in many papers in terms of band theory. Stefanik et al. proposed that Pr-substitution for cerium forms discrete acceptor levels (Pr 4f) for the lightly doped ceria (below 10 at.%).[34,35] The discrete states are not capable of giving rise to considerable electronic conductivity. Lübke et al.[13] proposed that the Pr 4f states lie much closer to the O2p valence edge than the Ce 4f conduction band. At sufficiently high temperature, electrons in the O2p state will be thermally excited and subsequently localized in the Pr 4f states, resulting in formation of holes in the valence band. Furthermore, at high temperatures and/or decrease pO_2, oxygen is released from the lattice increasing the electron occupation of the Pr 4f states. Here, we shall analyze the experimental results in a "chemical picture" relating the conduction to electronic defects associated with the Pr sites.

In several studies,[17,20,25] it has been reported that the electronic conductivity of Pr-doped ceria can be well described by a small polaron mechanism. Hence, mobility and conductivity will scale with temperature according to:[34]

$$\mu_{polaron} = \frac{(1 - [Pr'_{Pr}])ea^2\nu_0}{kT} \exp\left(-\frac{E_H}{kT}\right) \quad [18]$$

$$\sigma_{polaron} = N[Pr'_{Pr}]\mu_{polaron}e \quad [19]$$

$$\sigma_{polaron} = N[Pr'_{Pr}](1 - [Pr'_{Pr}])\frac{e^2a^2\nu_0}{kT} \exp\left(-\frac{E_H}{kT}\right) \quad [20]$$

$$[Pr'_{Pr}] = \frac{[Pr^{3+}]}{[Pr^{3+}] + [Pr^{4+}]} \quad [21]$$

where $\mu_{polaron}$ is the mobility of the small polaron, $[Pr'_{Ce}]$ is the fractional occupancy of electrons trapped on Pr ions. $[Pr^{3+}]$ is the concentration of trivalent Pr, N is the volumetric density of Pr atoms in the material (mol cm^{-3}). ν_0 is the jump frequency, E_H is the activation energy for hopping of the electron hole (electron hole migration), and a is the hopping distance. Eq. 20 can be rewritten to a simpler Arrhenius type expression;

$$\ln(\sigma_{polaron}T) = -\frac{E_H}{k}\frac{1}{T} + \ln C \quad [22]$$

where C is ($C = Ne^2[Pr'_{Pr}](1 - [Pr'_{Pr}])k^{-1}a^2\nu_0$). The electronic conductivity is thus influenced by both the concentration of Pr^{3+} and Pr^{4+}. When the concentration of Pr^{3+} prevails the material is a p-type conductor; where concentration of Pr^{4+} prevails it becomes n-type. In the following discussion we concentrate on the p-type electronic conductivity which is typically observed under practically realizable conditions. For comparison of mobilities and activation energies between the compositions we shall compare data at a fixed Pr^{3+}/Pr^{4+} ratio. The choice of 2.7 for Pr^{3+}/Pr^{4+} ratio relates the available pO_2 range for achieving a fixed ratio at all temperatures for all compositions. The oxygen partial pressures in equilibrium with a fixed ratio of ($Pr^{3+}/Pr^{4+} \approx 2.7$ as observed by TGA) in the different samples are listed in Table IV.

Fig. 12A shows Arrhenius plots of electronic conductivity with a fixed Pr^{3+}/Pr^{4+} ratio and corresponding linear fittings. The activation energies and pre-exponential constants of electronic conductivity obtained by linear fittings in Fig. 12A are shown in Figs. 12C and 12D, respectively. As indicated by Eq. 21, the activation energy in Fig. 12C corresponds to the migration enthalpy of the electron hole whilst the pre-exponential factor is associated with the jump frequency ν_0, hopping distance a and doping level. A noticeable feature in Fig. 12B is that there is a marked change in the scaling of the logarithm of the conductivity versus the Pr concentration around 10 at.% Pr especially at low temperature. An abrupt decline of the activation energy (Fig. 12C) and pre-exponential factor (Fig. 12D) is observed in the same x range.

Table IV. Oxygen partial pressure for the fixed ratio between Pr^{3+} and Pr^{4+} ($Pr^{3+}/Pr^{4+} = 2.7$) of CPGO at 700, 800 and 900°C.

Temperature /°C	900	800	700
CPGO40	1.70 bar	0.08 bar	9.0e-3 bar
CPGO30	0.76 bar	0.04 bar	5.6e-4 bar
CPGO25	0.20 bar	0.01 bar	5.0e-4 bar
CPGO15	0.10 bar	8.9e-4 bar	2.5e-5 bar

The Pr-doped CGO solid solutions can be viewed as PrO_x clusters homogenously embedded in the $Gd_{0.1}Ce_{0.9}O_{1.95-\delta}$ matrix. Electronic charge carriers (electrons or holes) are localized preferentially in the PrO_x units and migrate via them upon thermal excitation. For samples doped with low Pr concentration, the distance among the discrete PrO_x clusters is relatively long imposing a high energy barrier for electrons to jump across the CeO_2/Gd_2O_3-based zones, which are electronic "insulating". This results in low electronic conductivity and high activation energy for $x<0.1$ samples, as shown in Fig. 12C. Furthermore, the high value of the pre-exponential constant for the $0<x<0.1$ samples is indicative of a long electron hole hopping distance (a in Eq. 19).

As the dopant concentration increases, the distance between the Pr ions decreases, resulting in decreased effective hopping distance and decreased activation energy. The transient behavior in the range $0.08<x<0.15$ is akin to the percolation effect that is generally found in composite materials consisting of an electrical conductor and an insulator. That is, the abrupt increase of electrical conductivity occurs when the amount of the electrical conductor surpasses the percolation threshold above which a continuous electrical conduction pathway penetrates all the way through the composite. The same phenomenon is observed also in solid solutions. Swider and Worrell[45] employed a percolation model to explain the n-type electronic conductivity of Ti-doped YSZ. A theoretical percolation threshold of 12.5% for Ti-YSZ was proposed on the basis of bond percolation in the crystal structure. Kim et al.[46] recently developed a simple cubic percolation model to interpret the non-linear increment of electrical conductivity in perovskite structured $BaZrO_3$-$BaFeO_3$ solutions. Generally, the percolation threshold (Pc) for a close-packed crystal structure e.g. FCC is a function of the site coordination number Z, and can be simply evaluated as[47]

$$P_c = \frac{1.5}{Z} \quad [23]$$

The shortest possible jump distance will be achieved when the electronic defect localized on a given Pr dopant located on a corner of the cubic unit cell has at least one other Pr among the 12 nearest neighbor sites on the cubic face centers. A possible percolating Pr-Pr pathway is illustrated in Fig. 13. The cation coordination number in the FCC structure equals 12 ($Z = 12$ in Eq. 23). Therefore, by the simple model described in Ref. 47, the percolation threshold is ~12.5%, which means that the electronic defect may hop continuously among nearest Pr cations when 12.5% of the cation sites are occupied by Pr. The observed transition range (8 at.% −15 at.%) lies close to the one predicted by this simple percolation model. From the conductivity data plotted in Fig. 12 it is evident that a strong correlation exists between the structural connectivity of the Pr dopants and the migration enthalpy for the electron holes.

Due to the influence of activation energy and the pre-exponential factor, we herein plot the extrapolated conductivity at high temperature (e.g. 800°C) to pinpoint the abrupt change of electrical

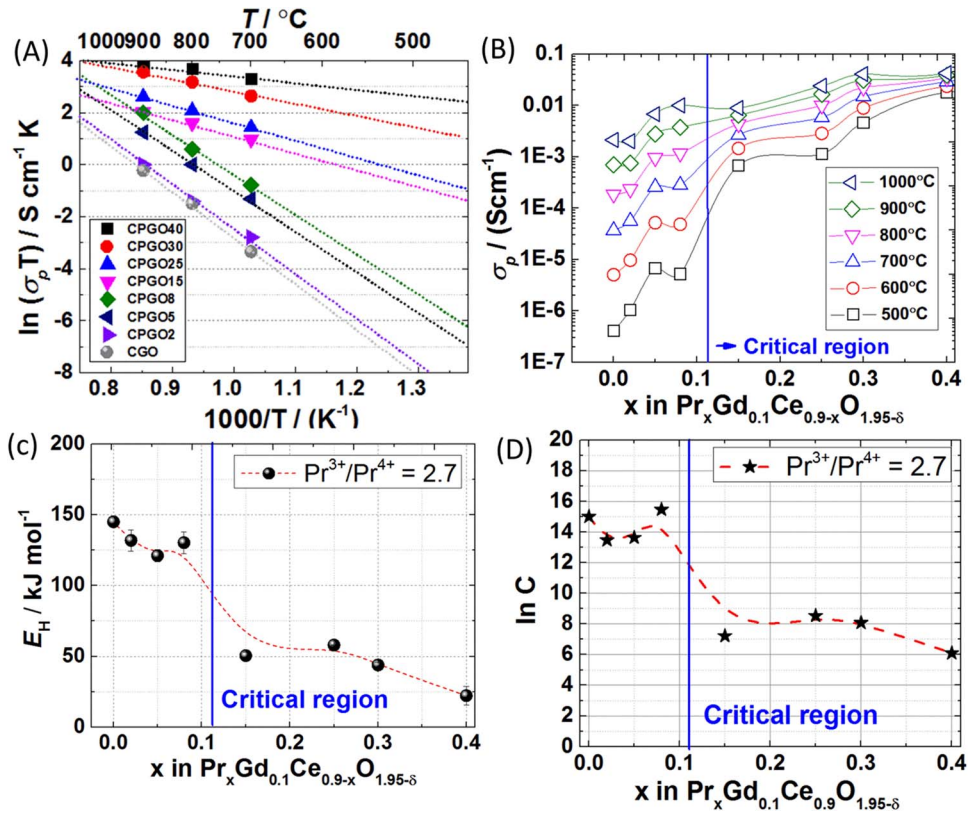

Figure 12. (A) Arrhenius plots of the electronic conductivity for CPGOx at a fixed Pr^{3+}/Pr^{4+}. (B) Electronic conductivity as a function of dopant concentration from 500°C to 1000°C. Apparent activation energy and (D) pre-exponential factor of the electronic conductivity versus x obtained from the linear fitting in (A). The dotted lines are plotted to guide the eye. The vertical line indicates a percolation threshold for Pr in the structure (see text).

conductivity arising from the migration enthalpy. In Fig. 14, the extrapolated electronic conductivity at 800°C was fitted by the percolation model proposed by Kim et al.[46] In this model, the conductivity for x<Pc and x>Pc is phenomenologically described by the expressions:

$$\text{For } x < P_c,\ \sigma(x) = \sigma_{GCO} x^{1/2} (P_c - x)^{-s} \quad [24]$$

$$\text{For } x > P_c,\ \sigma(x) = \sigma_{\mathrm{Pr}O_x} (x - P_c)^{t} \quad [25]$$

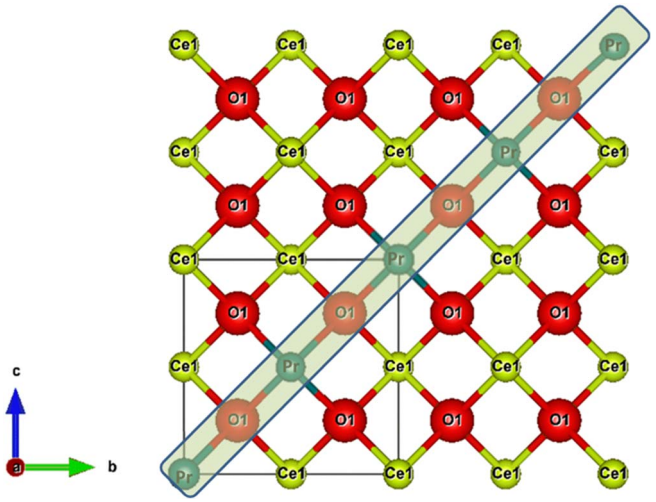

Figure 13. Schematic illustration of a (100) plane of a 2 × 2 matrix. A possible percolation path of Pr-Pr nearest neighbors is also shown.

where *s* and *t* are the universal size scaling exponents for the non-percolation matrix and the percolation phase, respectively. σ_{GCO} and $\sigma_{\mathrm{Pr}O_x}$ are the electronic conductivities of CGO and PrO_x[44] at 700°C, respectively. *Pc* is the percolation threshold being treated as a fitting parameter. *s* and *t* are the two fitting parameters where *t* is theoretically limited to lie in the range from 1.65 to 2 for the simple cubic percolation model. The best fit of the model to the data in Fig. 14 gives $t = 1.80$, $Pc = 0.125$ and $s = -1.11$, with the R^2 equals to 0.93. The model seems to satisfactorily fit the data in this work, which further elucidates that the electronic behavior can be well explained by the percolation model.

Chemical expansion (CE) under oxidizing conditions.—The chemical expansion of CGPO is related to the volumetric dilation upon changes in oxygen stoichiometry. The cell lattice parameter expands with the increase of the concentration of Pr^{3+}. Chatzichristodoulou et al.[37] has estimated that when relating unit cell volumes to the ionic radii of the constituting ions the size of an oxide vacancy in fluorites is smaller than that of the oxide ions. The chemical expansion of CPGO is thus in this picture a consequence of lattice dilation due to the increased radius of the cations partially counterbalanced with oxygen vacancy induced lattice contraction. The lattice parameter as calculated by Kim's formula includes the sum of the two effects. The relative chemical expansion can be simply calculated by a Vegard's law type relationship between lattice dimension and fraction of Pr^{3+} or Pr^{4+} in CPGO:

$$\varepsilon_{cal,chem} = \frac{\left[\mathrm{Pr}'_{\mathrm{Pr}}\right] a_{\mathrm{Pr}^{3+}} + \left(1 - \left[\mathrm{Pr}'_{\mathrm{Pr}}\right]\right) a_{\mathrm{Pr}^{4+}} - a_{XRD}}{a_{XRD}} \quad [26]$$

where $a_{\mathrm{Pr}^{3+}}$ and $a_{\mathrm{Pr}^{3+}}$ are the calculated lattice parameters for only Pr^{3+} or Pr^{4+}in CPGO, respectively (see Fig. 5). a_{XRD} is the lattice parameter obtained by XRD refinement (cf. Fig. 6), $[\mathrm{Pr}'_{\mathrm{Pr}}]$ is the fraction

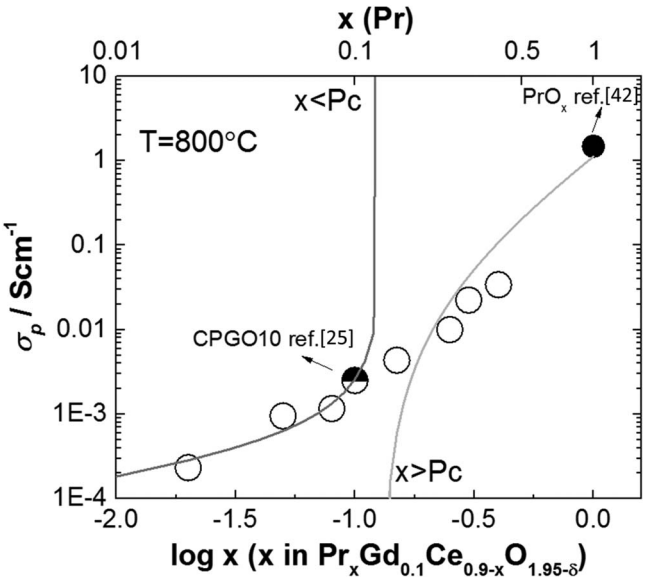

Figure 14. Electronic conductivity (fixed $Pr^{3+}/Pr^{4+} = 2.7$) at 800°C as a function of x. The data is fitted with a simple cubic percolation with charge carriers donated by dopants (Eq.24 and 25). The percolation threshold (P_c) is estimated to be x≈0.13 in the fitting. The electronic conductivity of CPGO10 ($Pr_{0.1}Gd_{0.1}Ce_{0.8}O_{1.95}$) and PrO_x are taken from Ref. 25 and Ref. 44 respectively.

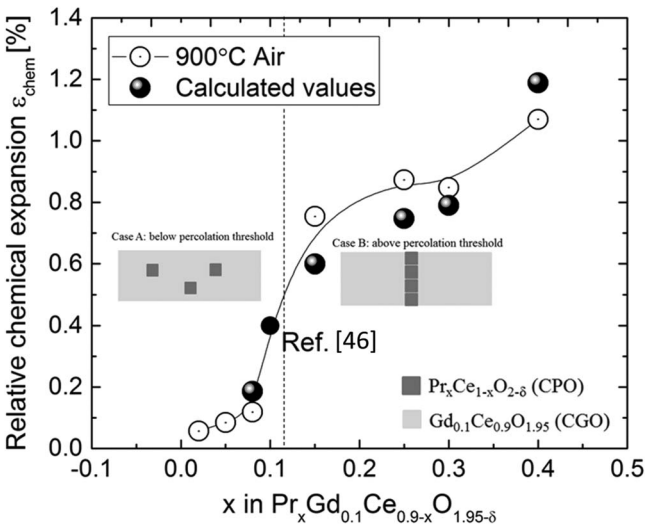

Figure 15. Dependence of relative chemical expansion on x in $Pr_xGd_{0.1}Ce_{0.9-x}O_{1.95-\delta}$. Calculated values of relative chemical expansion using Kim's formula in conjunction with thermodynamic parameters are also shown. The value of $Pr_{0.1}Gd_{0.1}Ce_{0.8}O_{1.95}$ calculated by Heidenreich et al.[48] is also included.

of Pr^{3+} calculated by the thermodynamic parameters outlined in Table II. Fig. 15 shows the relative chemical expansion (CE) from the experimental dilatometry data and the CE calculated by Eq. 24. Overall, the calculated CE in this simple model reproduces the general trend of the experimentally deduced CE well. Note that Eq. 26 is consistent with a type of expression as Eq. 16 i.e. it predicts proportionality between ε_{chem} and δ.

A transition is seen experimentally around 12.5% Pr. Below this the chemical expansion is small, above stronger. There are three reasons for this as seen when comparing the experimental data to the curve calculated from Eq. 26 and considering the ΔH, ΔS and β values reported in Tables II and III. Firstly; the overall expansion will increase with the fraction of the cation sites that are occupied by Pr (Fig. 5). Secondly, for a given T, pO_2 condition (900°C, air) the fraction of the Pr that is reduced increases with increasing Pr concentration (see Table II and Fig. 6). Thirdly, there is a weak tendency that above the percolation threshold the lattice responds even stronger to the change in ionic radius than below the threshold (the experimental data lies above the Eq. 26 trend line for x = 15, 25 and 30 but below for x = 8). It should be noted, that the relative chemical expansions listed in Fig. 15 are estimates only and thus encompassed with some uncertainties. They are derived from the measured total expansion (well determined) by subtracting an estimated thermal expansion, which is calculated under assumption of a constant thermal expansion coefficient (α) (see discussion in Thermal expansion section).

Besides the uncertainty introduced by this assumption, the data for the low Pr contents may be encompassed with an uncertainty due to incomplete equilibration with the atmosphere during the temperature sweeps. For these samples full oxygen equilibration, which is limited by electronic conductivity, might not have been achieved at the given cooling rate. This would add to exaggerate the change in behavior around the percolation threshold.

Electronic conductivity under reducing conditions.—Consistently, all the samples show n-type electronic conductivity under reducing conditions ($<1 \times 10^{-15}$ bar). The n-type regime is associated with partial reduction of Ce^{4+} as described in Eq. 4. However, for the

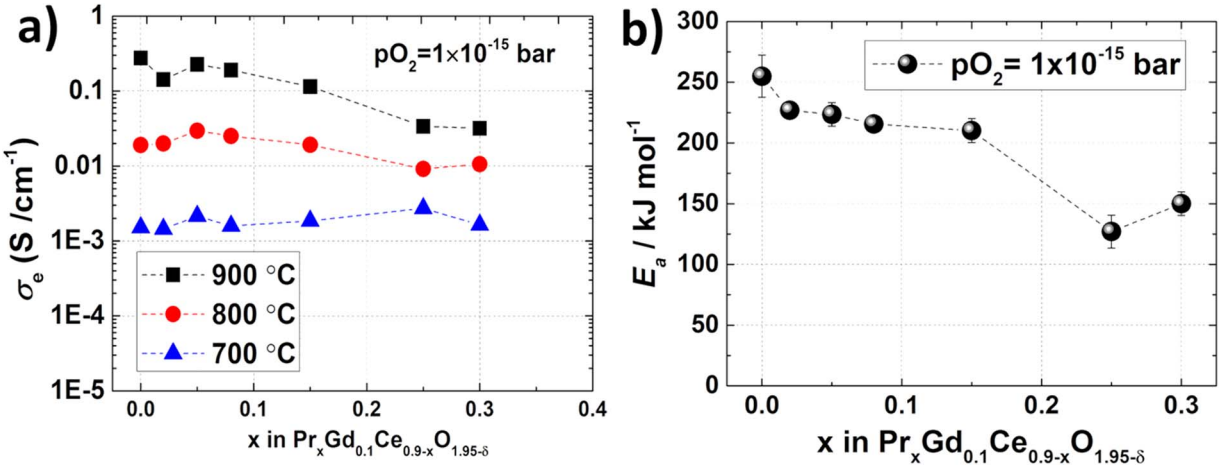

Figure 16. (a) *n*-type electronic conductivity of CPGO under $pO_2 = 1 \times 10^{-15}$ bar as a function of x at 700, 800 and 900°C. (b) Apparent activation energy of the electronic conductivity under $pO_2 = 1 \times 10^{-15}$ bar.

samples with high Pr concentration, the n-type electronic conductivity is partly overshadowed by the considerable p-type electronic conductivity (Fig. 9). The "net" n-type electronic conductivity at a given pO_2 (1×10^{-15} bar) is thus obtained by subtracting the extrapolated p-type electronic conductivity based on the slope of the p-type at high pO_2 branch from the total electronic conductivity. It is observed that the apparent activation energy of "net" n-type electronic conductivity decreases with increasing Pr concentration. Lübke et al.[13] found a slight decrease of the activation energy in CGO doped with 3 at.% Pr relative to that in CGO. Navarro et al.[49] also found that the 2 at.% Pr-doped CGO20 shows slightly decreased n-type conductivity relative to CGO20, in agreement with our results. In contrast to the trend observed in the pO_2 range dominated by p-type electronic conductivity, the n-type electronic conductivity under reducing conditions steadily decreases with increasing Pr concentration. The decrease of n-type electronic conductivity is more pronounced at high temperature (900°C). It is generally agreed that the n-type electronic conductivity in ceria is correlated with the electron hopping on the ceria sites (Ce^{3+}/Ce^{4+}). The mobility will thus be proportional to the concentration of Ce.[22] Here, partial substitution of Pr for Ce decreases the concentration of ceria (Ce^{3+}/Ce^{4+}), accounting for the lower n-type electronic conductivity because of the decreased number of sites. Under strongly reducing conditions, Pr^{4+} is completely reduced to Pr^{3+} which increases the oxygen vacancy concentration owing to the summation of now two acceptor dopants ($[Pr'_{Ce}]$ and $[Gd'_{Ce}]$). The high oxygen vacancy concentration is further unfavorable to the electron migration,[50,51] resulting from the more severe association between Ce'_{Ce} and $V_O^{\bullet\bullet}$ upon a larger oxygen vacancy concentration.[52] This effect also contributes to the reduction of the n-type conductivity in the Pr-containing samples.

The activation energy of the n-type electronic conductivity was also observed to decrease with increasing Pr concentration. The apparent activation energy is composed of two terms: $E = H_m + 1/4H_{Ce}$ where H_m is the enthalpy of electron migration and H_{Ce} is the standard reaction enthalpy. According to literature,[52] the enthalpy of electron migration increases with increasing oxygen vacancy concentration in ceria. Although H_m of the materials in this work is not known, increased H_m values are expected with increasing Pr concentration. This indicates that Ce will be more readily reduced upon a higher Pr concentration. A similar trend was also observed in purely Pr-doped ceria[35] and purely Gd-doped ceria.[53] It is also found that the reducibility of Ce^{4+} and Pr^{4+} in ceria tends to be facilitated by the increasing oxygen nonstoichiometry, leading to a non-ideal reduction behavior.[16] We herein attribute the decreased enthalpy of reduction of Ce to the high oxygen nonstoichiometry in heavily Pr-doped CGO.

Ionic conductivity.—For Pr and Gd co-doped ceria, more oxygen vacancies will form to compensate the increased concentration of negatively (compared to Ce^{4+}) charged aliovalent dopants (Pr'_{Ce} and Gd'_{Ce}). In analogy with purely Pr-doped or Gd-doped ceria,[3] the ionic conductivity of Pr and Gd co-doped ceria does not monotonously increase with increasing oxygen vacancy concentration as illustrated in Fig. 17. Instead, a maximum ionic conductivity occurs around an acceptor dopant concentration of 25 at.% (11.4 at% Pr^{3+}, 3.6 at.%Pr^{4+}, 10 at.% Gd and volumetric oxygen vacancy concentration equals to 1.07×10^{22} cm^{-3}). According to Dholabhai's DFT calculations,[54] 20 at. % dopant content in ceria shows the maximum ionic conductivity for 10 at.% Pr and 10 at.% Gd co-doped ceria, in good agreement with the experimental results in this work. Another noticeable feature is that the decrease of oxide ion conductivity above 25 at.% is associated with an increase in the apparent activation energy. The large activation energy of the electrical conductivity in heavily acceptor doped ceria is observed in several studies.[3,55] It is likely due to the association between the extrinsic dopants and oxygen vacancies;[55]

$$2Acc'_{Ce} + V_O^{\bullet\bullet} \rightarrow \left[Acc'_{Ce} V_O^{\bullet\bullet} Acc'_{Ce}\right] \text{ or}$$

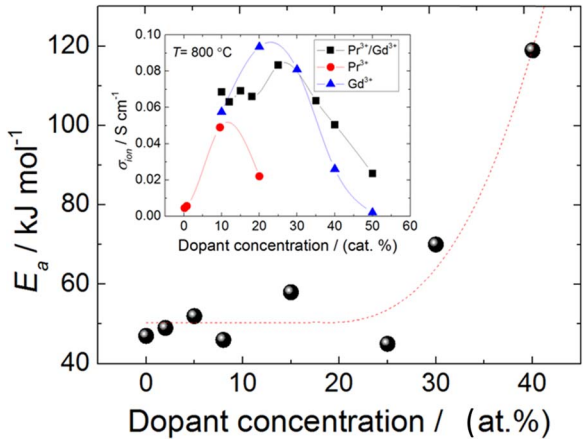

Figure 17. Apparent activation energies of oxide ion conductivity in pure N_2 ($pO_2 \approx 0.001$ bar) as a function of Pr content. The lines were plotted to guide the eye. Inset: The oxide ion conductivity measured at 800°C as a function of acceptor dopant concentration for different ceria solid solutions from Refs. 35,56,57. The ratio of Pr^{3+}/Pr^{4+} at 800°C in N_2 is in the range of 4–9.

$$Acc'_{Ce} + V_O^{\bullet\bullet} \rightarrow \left[Acc'_{Ce} V_O^{\bullet\bullet}\right]'$$

where Acc'_{Ce} represents the acceptor dopants Gd'_{Ce} and Pr'_{Ce} whereby some of the oxygen vacancies are trapped by the immobile dopants. As illustrated in Fig. 17, where the data for several different acceptor doped ceria compounds are compared, the defect association results in an increased apparent activation energy for oxide ion conductivity for the heavily doped samples.

Oxygen permeation flux.—The maximum achievable oxygen flux occurs when the oxide ion and electronic conductivity in a MIEC are both high and equal (transport number = 0.5). As shown in Fig. 18a where calculated transport numbers are shown, the transport number of CPGO approaches to 0.5 when the Pr concentration is in the range from 30 at.% to 40 at.%. Shuk et al.[58] also found nearly equal electronic and ionic conductivity for $Pr_{0.3}Ce_{0.7}O_{1.85-\delta}$ at 700°C, in good agreement with this work. The maximum achievable theoretical oxygen permeation flux can be calculated in terms of electronic and ionic conductivity using the Wagner's equation:

$$J_{O_2} = \frac{RT}{16F^2L} \int_{\ln pO_2''}^{\ln pO_2'} \frac{\sigma_e \sigma_i}{\sigma_e + \sigma_i} \partial \ln pO_2 \qquad [27]$$

The calculated oxygen permeation flux (here any losses at the two surfaces are neglected) follows the trend of t_e (Fig. 18b), due to the fact that the oxygen permeation flux of $Pr_xGd_{0.1}Ce_{0.9}O_{1.95-\delta}$ is dominantly limited by the electronic conductivity until a Pr concentration of approximately 40 at.%, where the maximum oxygen permeation flux is predicted for the here considered composition range (0–40 at.% Pr). Despite the reduced ionic conductivity when exceeding 25 at.% doping concentration, considering the bulk diffusion exclusively, the maximum oxygen flux for a 10-μm thick $Pr_{0.4}Gd_{0.1}Ce_{0.9}O_{1.95-\delta}$ based membrane may reach up to 10 Nml cm^{-2} min^{-1} at 800°C under the driving force of 0.21 bar/0.001 bar approaching the required level for being commercially interesting.[59] However, the considerable chemical expansion of CPGO40 (Fig. 7) is a severe challenge in terms of ensuring mechanical integrity and limits the applicability of the material.[8] To reduce risks of mechanical failure originating from chemical strain, very low thickness (1–10 μm) would be needed and the oxygen pressure gradient over the materials should be carefully controlled. A discussion of the consequence of chemical strain in supported membrane architectures can be found in Ref. 60–63.

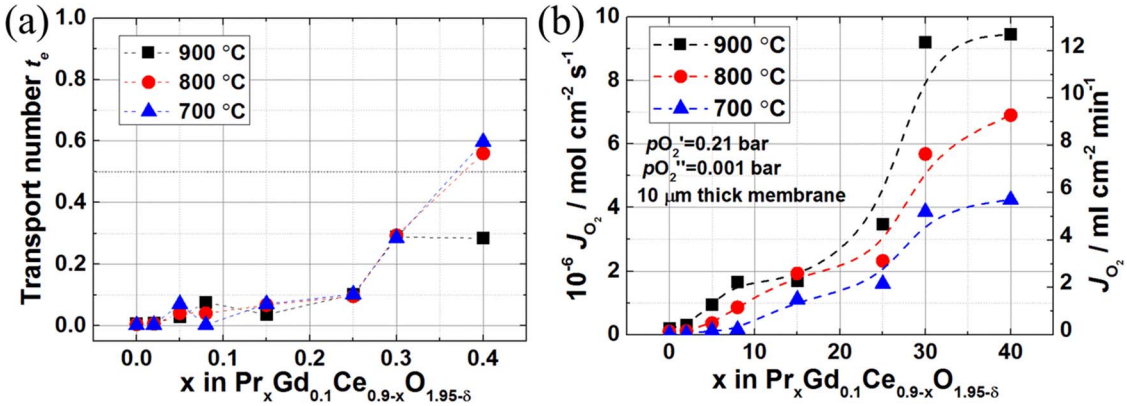

Figure 18. (a) Calculated transport number and (b) calculated oxygen permeation flux as a function of x in $Pr_xGd_{0.1}Ce_{0.9-x}O_{1.95-\delta}$ at 700, 800 and 900°C.

Conclusions

The investigations of the transport properties of Pr,Gd-doped ceria presented here has led to the following conclusions;

1. Doping Pr in CGO ($Pr_xGd_{0.1}Ce_{0.9-x}O_{1.95-\delta}$) significantly enhances the electronic conductivity (0.04 Scm^{-1} for $Pr_{0.4}Gd_{0.1}Ce_{0.5}O_{1.95-\delta}$ vs. 5.6 × 10^{-4} Scm^{-1} for $Gd_{0.1}Ce_{0.9}O_{1.95-\delta}$ at 900°C when pO_2 = 0.21 bar) under high oxygen partial pressures ($pO_2 > 10^{-8}$) and decreases slightly the n-type electronic conductivity (0.03 Scm^{-1} for $Pr_{0.4}Gd_{0.1}Ce_{0.5}O_{1.95-\delta}$ vs. 0.3 Scm^{-1} for $Gd_{0.1}Ce_{0.9}O_{1.95-\delta}$ at 900°C when pO_2 = 1 × 10^{-15} bar) under low oxygen partial pressures ($pO_2 < 10^{-8}$).
2. Doping Pr in CGO (10 at.% Gd) leads to a slight enhancement of the maximum oxide ion conductivity when the total dopant concentration is lower than 30 at.% (0.083 Scm^{-1} for $Pr_{0.15}Gd_{0.1}Ce_{0.75}O_{1.95-\delta}$ vs. 0.067 Scm^{-1} for $Gd_{0.1}Ce_{0.9}O_{1.95-\delta}$ at 800°C when pO_2 = 1 × 10^{-3} bar).
3. The apparent thermal expansion increases with increasing Pr concentration, due to increased chemical expansion (14.5 × 10^{-6} K^{-1} for $Pr_{0.05}Gd_{0.1}Ce_{0.85}O_{1.95-\delta}$ vs. 12.5 × 10^{-6} K^{-1} for $Gd_{0.1}Ce_{0.9}O_{1.95-\delta}$ in the range from 200°C to 900°C). The chemical expansion coefficient varies in the range from 0.05 to 0.09.
4. The enthalpy of the Pr^{4+} to Pr^{3+} reduction reaction decreases with increasing Pr concentration (112 ± 10 kJ mol^{-1} for $Pr_{0.4}Gd_{0.1}Ce_{0.5}O_{1.95-\delta}$ vs. 200 ± 34 kJ mol^{-1} for $Pr_{0.08}Gd_{0.1}Ce_{0.82}O_{1.95-\delta}$).
5. An abrupt decrease of the electron hole migration enthalpy is observed when the Pr concentration increases from 8 to 15 at.%, which is likely associated with the establishment of a percolation path between the Pr atoms as the chance of finding a continuous path of Pr atoms in the nearest neighbor positions strongly increases at this substitution level. The percolation threshold can be interpreted in a simple cubic percolation model.
6. No beneficial effect of adding 3% Co to the achievable permeation flux is observed but the Co is found to be a good sintering aid.
7. The Gd/Pr co-doped material may be applied in composite electrodes (SOFC cathodes) where the simultaneous increase in ionic and electronic conductivity on Pr substitution in the CGO will be beneficial and the large chemical expansion may be tolerable if only used in nanoparticulate form. The large chemical expansion introduced by the co-doping limits application for membranes, as to bring the electronic conductivity in the range of the ionic one needs more than 12.5 at.% Pr addition, which also makes the material prone to problems related to the large chemical (stoichiometric) expansion.
8. The achievable oxygen permeation flux of CGO is enhanced by co-doping with Pr because of the enhanced electronic conductivity. CPGO40 is predicted to show the largest achievable flux as the electronic conductivity approaches the ionic one. As a trade-off, CPGO5 is a promising material for OTMs in terms of enhanced oxygen flux and low chemical expansion.

Acknowledgments

The authors thank DSF (Danish council for Strategic Research) for the finical support on the project "ENEFOX"- Energy Efficient Oxygen Production for a Sustainable Energy System". (11–116387). We also acknowledge S. Bishop for pointing us to, that a percolation type behavior could be expected in the here investigated type of materials.

References

1. M. Puig-Arnavat, S. Soprani, M. Sogaard, K. Engelbrecht, J. Ahrenfeldt, U. B. Henriksen, and P. V. Hendriksen, *RSC Advances*, **3**, 20843 (2013).
2. M. P. Lobera, J. M. Serra, S. P. Foghmoes, M. Søgaard, and A. Kaiser, *Journal of Membrane Science*, **385**, 154 (2011).
3. M. Mogensen, N. M. Sammes, and G. A. Tompsett, *Solid State Ionics*, **129**, 63 (2000).
4. S. D. Ebbesen, S. H. Jensen, A. Hauch, and M. B. Mogensen, *Chemical reviews*, **114**, 10697 (2014).
5. W. C. Chueh, Y. Hao, W. Jung, and S. M. Haile, *Nat Mater*, **11**, 155 (2012).
6. S. Wang, T. Kobayashi, M. Dokiya, and T. Hashimoto, *Journal of The Electrochemical Society*, **147**, 3606 (2000).
7. C. Chatzichristodoulou, S. Ricote, S. P. V. Foghmoes, J. Glasscock, A. Kaiser, and P. V. Hendriksen, *Solid State Ionics*, **269**, 51 (2015).
8. A. Kaiser, S. Foghmoes, C. Chatzichristodoulou, M. Søgaard, J. A. Glasscock, H. L. Frandsen, and P. V. Hendriksen, *Journal of Membrane Science*, **378**, 51 (2011).
9. C. Chatzichristodoulou, J. Glasscock, A. Kaiser, S. P. V. Foghmoes, and P. V. Hendriksen, *J Electrochem Soc*, **158**, F73 (2011).
10. C. Chatzichristodoulou, M. Søgaard, and P. V. Hendriksen, *Journal of The Electrochemical Society*, **158**, F61 (2011).
11. P. S. Manning, J. D. Sirman, and J. A. Kilner, *Solid State Ionics*, **93**, 125 (1996).
12. J. A. Lane and J. A. Kilner, *Solid State Ionics*, **136**, 997 (2000).
13. S. Lübke and H. D. Wiemhöfer, *Solid State Ionics*, **117**, 229 (1999).
14. D. Fagg, V. Kharton, and J. Frade, *Journal of Electroceramics*, **9**, 199 (2002).
15. D. P. Fagg, J. C. C. Abrantes, D. Perez-Coll, P. Nunez, V. V. Kharton, and J. R. Frade, *Electrochimica Acta*, **48**, 1023 (2003).
16. C. Chatzichristodoulou, P. V. Hendriksen, and A. Hagen, *Journal of The Electrochemical Society*, **157**, B299 (2010).
17. M. Balaguer, C. Solís, and J. M. Serra, *Chem. Mater.*, **23**, 2333 (2011).
18. V. V. Kharton, A. P. Viskup, F. M. Figueiredo, E. N. Naumovich, A. L. Shaulo, and F. M. B. Marques, *Materials Letters*, **53**, 160 (2002).
19. S. R. Bishop, H. L. Tuller, Y. Kuru, and B. Yildiz, *Journal of the European Ceramic Society*, **31**, 2351 (2011).
20. C. Chatzichristodoulou and P. V. Hendriksen, *Journal of The Electrochemical Society*, **157**, B481 (2010).
21. S. R. Bishop, T. S. Stefanik, and H. L. Tuller, *Physical Chemistry Chemical Physics*, **13**, 10165 (2011).
22. S. Lübke and H. D. Wiemhöfer, *Berichte der Bunsengesellschaft für physikalische Chemie*, **102**, 642 (1998).
23. C. Chatzichristodoulou, S. Ricote, S. P. V. Foghmoes, J. Glasscock, A. Kaiser, and P. V. Hendriksen, *Solid State Ionics*, **269**, 51 (2015).
24. C. Chatzichristodoulou and P. V. Hendriksen, *Phys. Chem. Chem. Phys.*, **13**, 21558 (2011).
25. K. Schmale, M. Grünebaum, M. Janssen, S. Baumann, F. Schulze-Küppers, and H.-D. Wiemhöfer, *physica status solidi (b)*, **248**, 314 (2011).
26. I. Riess, *Solid State Ionics*, **91**, 221 (1996).

27. A. Kaiser, A. S. Prasad, S. P. Foghmoes, S. Ramousse, N. Bonanos, and V. Esposito, *Journal of the European Ceramic Society*, **33**, 549 (2013).
28. Y. Takasu, T. Sugino, and Y. Matsuda, *Journal of applied electrochemistry*, **14**, 79 (1984).
29. D.-J. Kim, *Journal of the American Ceramic Society*, **72**, 1415 (1989).
30. R. t. Shannon, *Acta Crystallographica Section A: Crystal Physics, Diffraction, Theoretical and General Crystallography*, **32**, 751 (1976).
31. J. D. McCullough, *Journal of the American Chemical Society*, **72**, 1386 (1949).
32. G. Zhou and R. J. Gorte, *Journal of Physical Chemistry B*, **112**, 9869 (2008).
33. G. S. Lewis, A. Atkinson, B. C. H. Steele, and J. Drennan, *Solid State Ionics*, 152, 567 (2002).
34. T. S. Stefanik, Electrical properties and defect structure of Praseohymium-Cerium Oxide Solid solutions, M. I. T PhD thesis (2004).
35. S. R. Bishop, T. S. Stefanik, and H. L. Tuller, *Journal of Materials Research*, **27**, 2009 (2012).
36. H. L. Tuller, S. R. Bishop, D. Chen, Y. Kuru, J. J. Kim, and T. S. Stefanik, *Solid State Ionics*, **225**, 194 (2012).
37. C. Chatzichristodoulou, P. Norby, P. V. Hendriksen, and M. B. Mogensen, *Journal of Electroceramics*, **34**, 100 (2014).
38. J. Newman, *Journal of The Electrochemical Society*, **113**, 501 (1966).
39. D. P. Fagg, I. P. Marozau, A. L. Shaula, V. V. Kharton, and J. R. Frade, *Journal of Solid State Chemistry*, **179**, 3347 (2006).
40. V. V. Kharton, A. P. Viskup, F. M. Figueiredo, E. N. Naumovich, A. A. Yaremchenko, and F. M. B. Marques, *Electrochimica Acta*, **46**, 2879 (2001).
41. C. Chatzichristodoulou, P. B. Tullmar, M. Søgaard, P. V. Hendriksen, and M. B. Mogensen, in *Catalysis by ceria and related materials*, World Scientific Publishing Co Pte Ltd (2013).
42. D. P. Fagg, S. García-Martin, V. V. Kharton, and J. R. Frade, *Chemistry of Materials*, **21**, 381 (2008).
43. V. V. Kharton, F. M. Figueiredo, L. Navarro, E. N. Naumovich, A. V. Kovalevsky, A. A. Yaremchenko, A. P. Viskup, A. Carneiro, F. M. B. Marques, and J. R. Frade, *Journal of Materials Science*, **36**, 1105 (2001).
44. V. Thangadurai, R. Huggins, and W. Weppner, *J Solid State Electrochem*, **5**, 531 (2001).
45. K. E. Swider and W. L. Worrell, *Journal of The Electrochemical Society*, **143**, 3706 (1996).
46. D. Kim, S. Miyoshi, T. Tsuchiya, and S. Yamaguchi, *Solid State Ionics*, **262**, 875 (2014).
47. R. Zallen, in *The Physics of Amorphous Solids*, p. 170, Wiley-VCH Verlag GmbH (2007).
48. M. Heidenreich, C. Kaps, A. Simon, F. Schulze-Küppers, and S. Baumann, *Solid State Ionics*, **283**, 56 (2015).
49. L. Navarro, F. Marques, and J. Frade, *Journal of The Electrochemical Society*, **144**, 267 (1997).
50. M. Mogensen, T. Lindegaard, U. R. Hansen, and G. Mogensen, *Journal of The Electrochemical Society*, **141**, 2122 (1994).
51. H. L. Tuller and A. S. Nowick, *Journal of The Electrochemical Society*, **126**, 209 (1979).
52. B. C. H. Steele, *Solid State Ionics*, **129**, 95 (2000).
53. S. Wang, H. Inaba, H. Tagawa, M. Dokiya, and T. Hashimoto, *Solid State Ionics*, **107**, 73 (1998).
54. P. P. Dholabhai, J. B. Adams, P. A. Crozier, and R. Sharma, *Journal of Materials Chemistry*, **21**, 18991 (2011).
55. H. J. Avila-Paredes, K. Choi, C.-T. Chen, and S. Kim, *Journal of Materials Chemistry*, **19**, 4837 (2009).
56. H. Yamamura, H. Nishino, K. Kakinuma, and K. Nomura, *Journal of the Ceramic Society of Japan*, **111**, 902 (2003).
57. T. Kudo and H. Obayashi, *Journal of The Electrochemical Society*, **123**, 415 (1976).
58. P. Shuk and M. Greenblatt, *Solid State Ionics*, **116**, 217 (1999).
59. R. Bredesen, K. Jordal, and O. Bolland, *Chem. Eng. Process.*, **43**, 1129 (2004).
60. P. V. Hendriksen, P. H. Larsen, M. Mogensen, F. W. Poulsen, and K. Wiik, *Catalyst Today*, **56**, 283 (2000).
61. P. V. Hendriksen, J. Høgsberg, A. M. Kjeldsen, B. F. Sørensen, and H. Pedersen, *Adv. in Solid Oxide Fuel Cells II, Ceramic Eng. and Science Proceedings*, **27**, 347 (2008).
62. K. Kwok, H. L. Frandsen, M. Søgaard, and P. V. Hendriksen, *Journal of Membrane Science*, **453**, 253 (2014).
63. K. Kwok, H. L. Frandsen, M. Søgaard, and P. V. Hendriksen, *Journal of Membrane Science*, **470**, 80 (2014).